Integration of Field Monitoring and Numerical Modelling to Evaluate the Construction Performance of a Deep-Sea Quay Wall

Fengwen Lai[1]; Kevin Duffy[2]; Ken Gavin[3]; Dechun Lu[4]; and Alfred Roubos[5]

Abstract: Quay walls are often assessed using numerical models to capture highly nonlinear soil behavior and the complex interactions between foundation elements. The input parameters of these models are usually derived from advanced laboratory tests; however, capturing the spatial variation in these properties across large quay walls can prove inefficient and costly. Moreover, the difficulty in performing full-scale load tests or small-scale physical models complicates the validation of the numerical model. This paper addresses these challenges by using monitoring data during the construction of a deep-sea quay wall in the Port of Rotterdam. The quay wall, installed primarily in sand, consists of an anchored retaining wall with a concrete relieving platform. During dredging in front of the wall, fiber optic sensors and inclinometers measured large changes in anchor forces and wall deflection. These changes were then compared to the predictions of a finite element model with the hardening soil model with small strain stiffness constitutive model, with the input parameters derived from cone penetration tests (CPT). The results from the CPT-based numerical model were in good agreement with the measured data, demonstrating the feasibility of integrating numerical modelling and field monitoring while supporting the use of the CPT to calibrate advanced soil constitutive models. The validated model provides a reliable basis against which hypothetical adaptation or remediation measures to the wall can be assessed, such as changes in the dredged seabed depth and surcharge loading. **DOI: 10.1061/JGGEFK.GTENG-13694.**

Author keywords: Quay wall; Field monitoring; Numerical modelling; Cone penetration test; Construction performance.

Introduction

Ports are an integral part of global trade, with maritime shipping accounting for around 80% of all global trade by volume (UNCTAD 2023). Global trade also continues to grow, increasing the demand for ports to accommodate for larger ships and more frequent port calls. Most ships berth alongside a quay wall, which is an earth-retaining structure designed to withstand berthing and mooring forces, as well as facilitating the handling and storage of goods. To tie these demands in with the constraints of the local soil and nautical conditions, a variety of different quay wall structures exist (De Gijt 2010), including gravity walls, sheet pile walls, open berth quays, and quay walls with relieving platforms.

While analytical modelling is an efficient means of designing simple retaining walls, the performance of many quay walls is governed by highly nonlinear soil behavior and complex soil–structure interaction mechanisms such as pile group effects, inclined retaining walls, and interactions between different foundation elements. Therefore, numerical modelling is often the tool of choice for quay wall design (Qiu and Grabe 2012; Roubos et al. 2021; Alesiani and Ruggeri 2024). Further, constitutive models such as the hardening soil model with small-strain stiffness (HSS), which is readily available in commercial software, can realistically capture the dependence of stiffness on the stress-strain levels (Schanz et al. 1999; Benz 2007; Lai et al. 2021, 2025a, b).

Inevitably, the accuracy of these constitutive models depends on the input parameters. While laboratory testing is the most direct means of obtaining these inputs, the results are often affected by sample disturbance, particularly in sandy soils. Further, to capture the full stiffness degradation response, relatively complex and expensive laboratory tests are required. Since quay walls can range from hundreds of meters to several kilometers in length, an advanced laboratory test program across the entire site is often prohibitive (Brinkgreve and Brasile 2022). In situ tests, such as the cone penetration test (CPT), provide a way of deriving input parameters with minimal disturbance and at high spatial resolutions. Therefore, a key focus of this study is the development of a rigorous yet practical CPT-based calibration approach of the HSS model parameters.

Yet even with rigorously developed model inputs, the numerical model should be validated by full-scale load tests. However, the cost and complexity of performing these tests on operational quay walls means this cannot often be performed, and only a small amount of cases are in public literature (Feremans and Vanhooydonck 2019; Hemel 2023; Alesiani and Ruggeri 2024). Nevertheless, with the increasing number of "smart quay walls" (Voogt 2023), the large

[1]Assistant Professor, College of Civil Engineering, Fuzhou Univ., Fuzhou 350108, China; formerly, Guest Researcher, Dept. of Geoscience and Engineering, Delft Univ. of Technology, Stevinweg 1, Delft 2628 CN, Netherlands (corresponding author). ORCID: https://orcid.org/0000-0002-9045-0659. Email: laifengwen@fzu.edu.cn

[2]Postdoctoral Researcher, Dept. of Geoscience and Engineering, Delft Univ. of Technology, Stevinweg 1, Delft 2628 CN, Netherlands. ORCID: https://orcid.org/0000-0002-7918-2171

[3]Professor of Subsurface Engineering, Dept. of Geoscience and Engineering, Delft Univ. of Technology, Stevinweg 1, Delft 2628 CN, Netherlands.

[4]Professor, Institute of Geotechnical and Underground Engineering, Beijing Univ. of Technology, Beijing 100124, China; Chair Professor, College of Civil Engineering, Fuzhou Univ., Fuzhou 350108, China.

[5]Senior Engineer, Port of Rotterdam Authority, Wilhelminakade 909, Rotterdam 3072 AP, Netherlands.

Note. This manuscript was submitted on November 24, 2024; approved on July 29, 2025; published online on October 8, 2025. Discussion period open until March 8, 2026; separate discussions must be submitted for individual papers. This paper is part of the ***Journal of Geotechnical and Geoenvironmental Engineering***, © ASCE, ISSN 1090-0241.

movements incurred by the construction process provides a means of validating the model predictions.

With this in mind, this paper presents a quay wall from the Port of Rotterdam, consisting of an anchored retaining wall with a relieving platform. A CPT-based approach was developed to determine a full set of the HSS model parameters, which was validated against high-quality laboratory and in situ tests. A finite element model was then established based on these input parameters and compared to the measured wall deflections and anchor forces during the dredging of soil in front of the wall. Using the validated model, hypothetical changes over the quay wall's lifetime are also considered, showing the influence of dredged seabed depth and surface loading on the anchor force and wall deflection.

Project Description

Quay Wall Overview

The Port of Rotterdam is Europe's largest port and has an important role in trade and offshore construction in the North Sea. As part of its ongoing expansion, a new 1.2 km long quay wall was constructed on a dredged peninsula known as the Maasvlakte. This paper considers a section of the quay wall referred to as Section B4 (Fig. 1), chosen because of the construction measurements available at the section and its representativeness of the quay wall and ground conditions as a whole. With a dredged depth of −24.5 m, Section B4 was designed for very large crude carriers (VLCC). Section A, 60 m to the west of Section B4, was designed for Suezmax classed ships, and so the dredged depth at Section A was 5.0 m shallower than Section B.

The retaining wall at Section B4 is a so-called "combined wall" (Fig. 2), wherein driven tubular piles (1.42 m outer diameter and 24 mm in thickness) installed at 3.3 m spacing provide most of the wall's horizontal stiffness. Sheet piles (PU28) then span the gap between the tubular piles, installed deep enough to prevent soil flow toward the seaside while minimizing the installation risks and cost associated with installing the sheet piles deeper into the very dense sand. A concrete superstructure lies above the combined wall, consisting of a relieving platform (16.8 m width and 2.0 m thickness) and a front wall (2.2 m width and 5.0 m height). The superstructure was cast in segments measuring 23 m in length and connected to one another using a keyed joint at the front wall and at the relieving platform. Each segment was then connected to the front of the tubular piles with a steel saddle, acting as a hinged connection (De Gijt and Broeken 2013). To anchor the retaining wall, steel H-beams (HEB 600) known as Müller Verpress anchors (MV piles), were installed using a combination of hammering and grout injection to a depth of −38.0 m and at an angle of 45°. To support the relieving platform, two rows of screw injection piles (SI piles) with a permanent casing were installed at an angle of 10° and to a depth of −33.0 m, as shown in Fig. 3. Table 1 gives the dimensions and mechanical parameters of the structural elements.

Ground Conditions

Before construction, nearly 200 CPTs and 15 boreholes were performed across the entire quay wall. Around Section B4 (Fig. 1), five CPTs were carried out on the waterside with an initial elevation of −4.0 m, and 10 CPTs on the landside with an initial elevation of +5.0 m. One borehole was also performed near the cross section.

The CPT profiles are shown in Fig. 4, including the cone resistance q_c, sleeve friction f_s, friction ratio R_f, along with the derived effective friction angle ϕ' and oedometer modulus E_{oed}. The site was divided into five ground units (GUs) based on these measurements, the site's geological history and the engineering relevance of each GU:

- GU1 (+5.0 to 0.0 m): Loose moderately coarse SAND, used as backfill after casting of superstructure.
- GU2 (0.0 to −13.0 m): Medium dense fine to coarse SAND, deposited during the creation of the Maasvlakte Peninsula in the 1960s.
- GU3 (−13.0 to −19.0 m): Medium dense to dense silty fine SAND (Holocene-era Echteld and Naaldwijk Formations), locally with clayey and silty pockets.
- GU4 (−19.0 to −22.0 m): Stiff CLAY (Wijchen Member, Kreftenheye Formation), deposited during the late-Pleistocene.

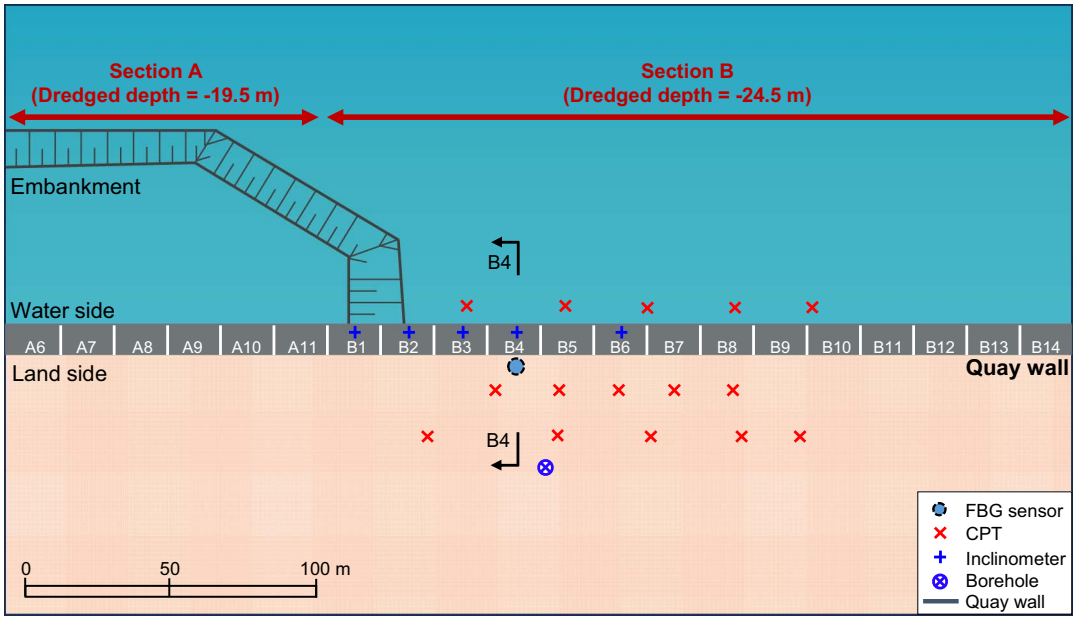

Fig. 1. Layout of site investigation and instrumentation within the region of interest (Section B4).

J. Geotech. Geoenviron. Eng., 2025, 151(12): 04025156

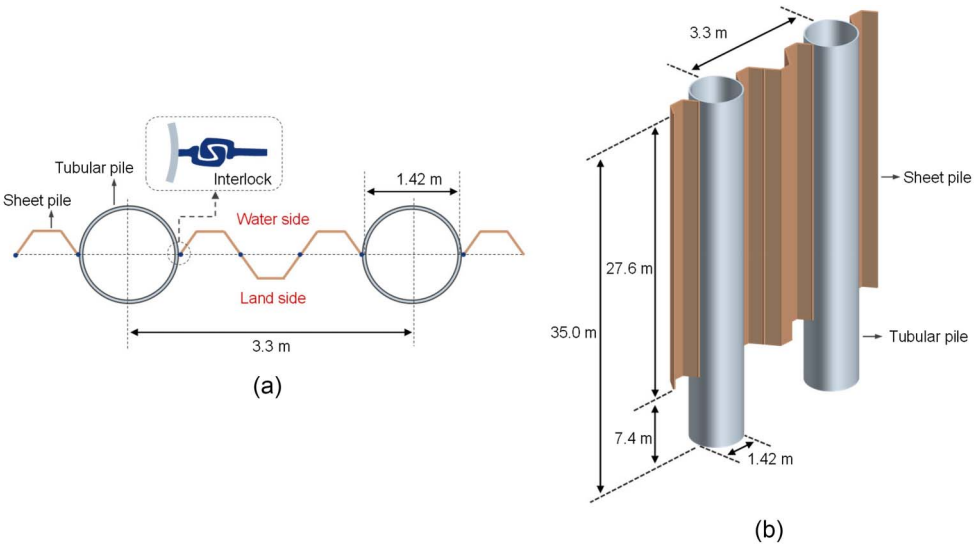

Fig. 2. Combined wall in: (a) top view; and (b) 3D view.

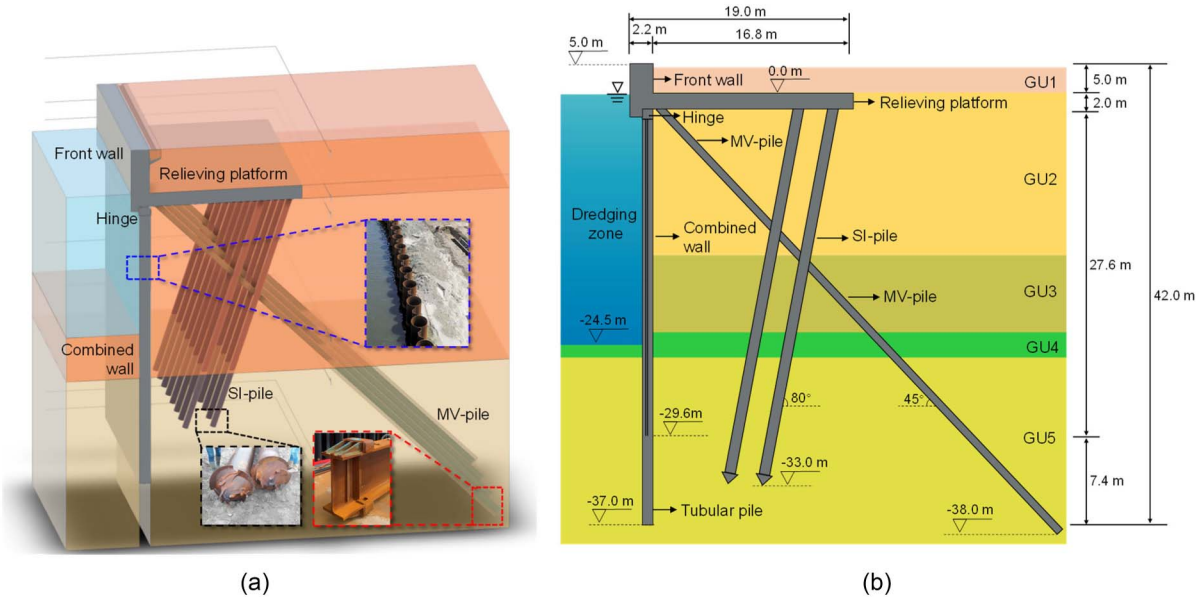

Fig. 3. (a) Structural elements of the quay wall in 3D view; and (b) geometric configuration of the quay wall.

Table 1. Parameters of the structural elements used in the quay wall

Structural type	Dimensions (m)	Center-to-center distance (m)	Embedded depth (m)	Material quality (-)	Young's modulus (GPa)
		Combined wall			
Tubular pile	$D_{inner} = 1.37$ $D_{outer} = 1.42$	3.3	−37.0	Steel: X71	210
Sheet pile (PU28)	Width = 1.80 Height = 0.50	3.3	−29.6	Steel: 355GPa	210
MV pile	Width = 0.30 Height = 0.30	3.8	−38.0	Steel: S420M	210
SI pile	$D_{tube} = 0.60$ $D_{tip} = 0.90$	Perpendicular to wall = 3.0 Parallel to wall = 3.3	−33.0	Steel: S355 J2H Concrete: C35/C45	Steel = 210 Concrete = 20
Relieving platform	Width = 16.80 Height = 1.80	—	0.0	Concrete: C35/C45	20
Front wall	Width: 2.20 Height: 7.00	—	−2.0	Concrete: C35/C45	20

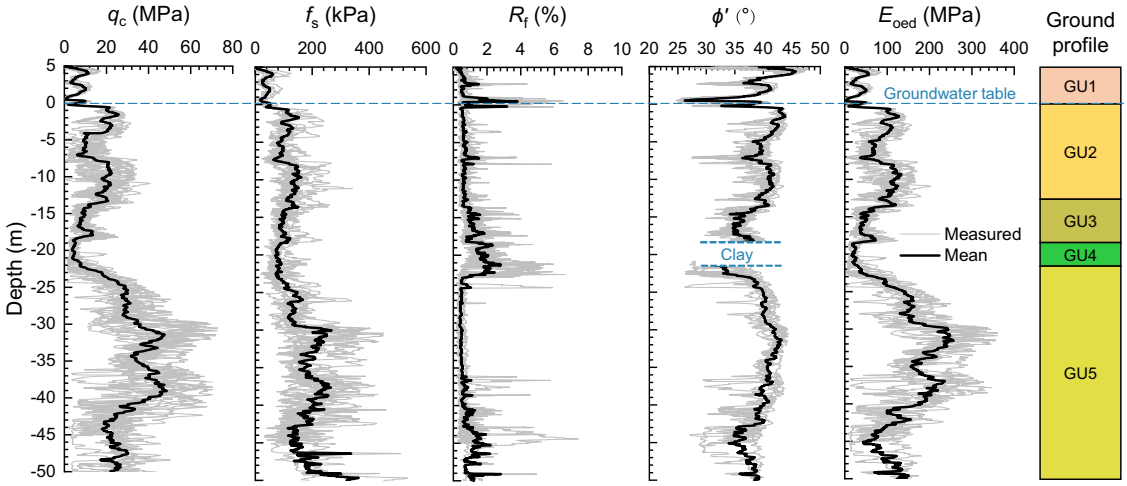

Fig. 4. CPT data and interpreted parameter profiles across the test site and the ground units.

- GU5 (−22.0 to −50 m): Dense to very dense slightly gravelly coarse SAND (Kreftenheye Formation), fluvially deposited during the late-Pleistocene era. Variation in lower boundary with moderately sandy clay layer from −40 to −50 m.

Construction Sequence

Construction of the quay wall at Section B4 lasted around 14 months and followed a phased approach [Figs. 5 and 6]. Prior to construction, there was a natural slope of 1:4 from 5.0 m depth to −24.5 m [Fig. 6(a)]. An embankment was then constructed to provide a platform for the piling rigs during the installation of the MV piles, SI piles, and the combined wall [Figs. 5(a and b)]. The concrete superstructure was then cast in 23 m long segments [Fig. 5(c)] and backfilled with sand (GU1). The soil in front of the quay wall was then incrementally dredged to the desired seabed depth, as shown in Fig. 6.

Field Monitoring

Lateral deformation of the combined wall and forces acting on the MV piles were measured during quay wall construction, providing a data set against which the numerical model could be validated. In total, 50 inclinometers were installed along the wall, and six MV piles were instrumented at the pile head.

The measurements available at Section B4 are presented in Fig. 7. The Roctest Telemac DIS-500 manual inclinometer (accuracy = ±2 mm per 25 m) measured the lateral deformation of the combined wall during construction. To do so, a small steel tube was welded to the outside of the tubular piles before installation. Inclination measurements were made at different dates during construction and dredging. After making the initial measurement on a given date, another measurement was made with the inclinometer rotated 180° for the second measurement to remove systematic errors (Stark and Choi 2008).

The MV piles were instrumented with fiber Bragg gratings (FBGs). FBGs measure the combined influence of strain and temperature by analyzing how light propagates through a series of gratings etched into an optical fiber. The change in returning wavelength is dependent on the strain and temperature across the gratings. The measured strains were subsequently converted to a normal force (F_{anchor}) using the Young's modulus of the pile (E = 200 GPa) and the pile's cross-sectional area (0.27 m^2).

Six FBGs were mounted at the head of each MV pile (Fig. 7) at a depth of −2.3 m, just below the relieving platform. Five sensors (L_{top}, R_{top}, L_{middle}, L_{bottom}, and R_{bottom}) were designated as axial strain sensors and were fixed to the flanges on both sides of the H-profile as well as in the middle of the web (L_{middle}). Each FBG was mounted into a thin steel plate, which was then glued and welded to the steel MV pile after installation. The gauges were then covered by another steel plate for mechanical protection

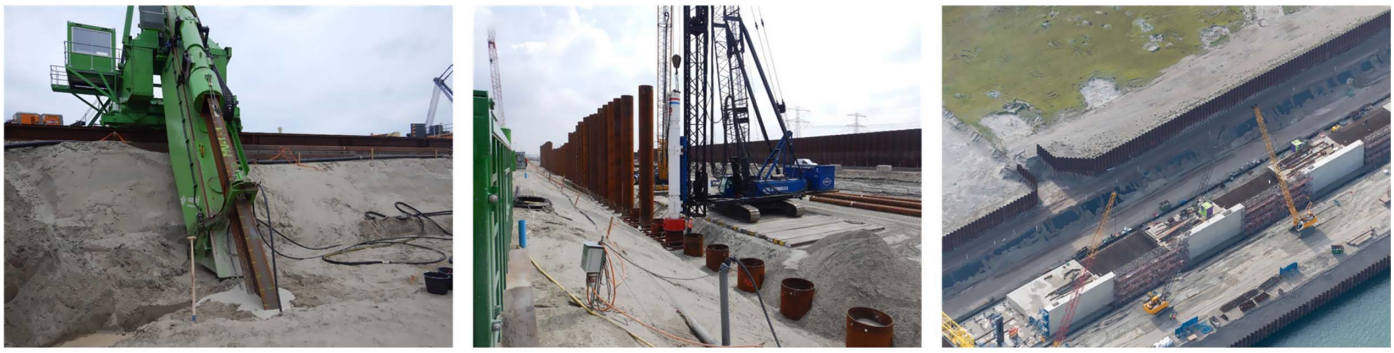

Fig. 5. Construction sequence of the quay wall: (a) installation of the MV piles; (b) installation of the combined wall; and (c) construction of the relieving platform. (Images courtesy of Port of Rotterdam Authority.)

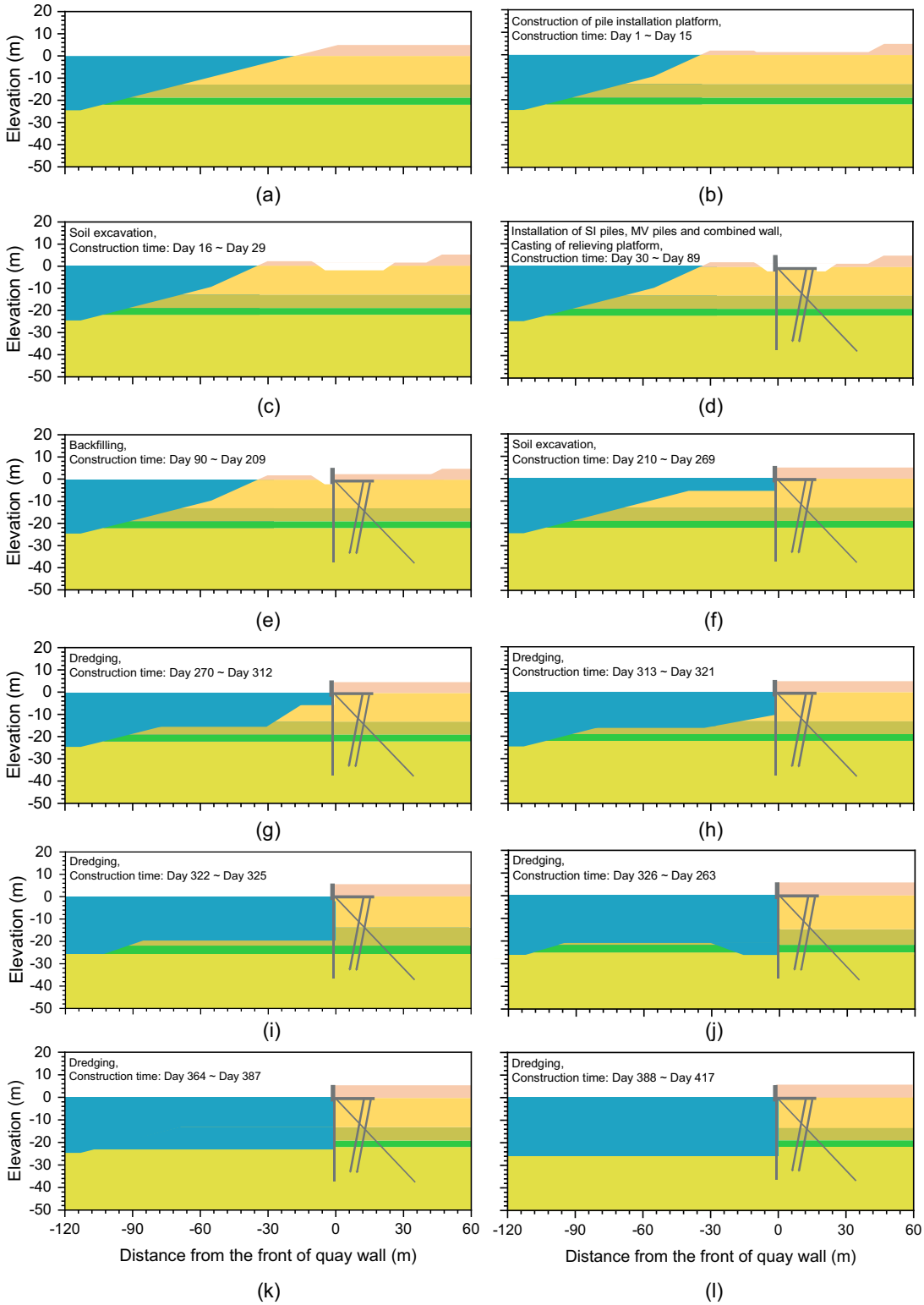

Fig. 6. Changes in the elevation for quay wall of Section B4 at: (a) initial phase; (b) Phase 1; (c) Phase 2; (d) Phases 3 & 4; (e) Phase 5; (f) Phase 6; (g) Phase 7a; (h) Phase 7b; (i) Phase 7c; (j) Phase 7d; (k) Phase 7e; and (l) Phase 7f.

and covered with a resin coating to prevent water ingress. One additional FBG (temp) was placed in a mounting that isolated it from any mechanical strain and could be used to thermally compensate the measurements from the strain sensors as per Kim et al. (2017). Once operating, the FBGs measured at a frequency of once every hour.

As an example, Fig. 8 compares the changes in measured strains in the MV pile in response to dredging in front of the quay wall of Section B4. Most of the strains develop in the first five stages of dredging, where the seabed level in front of the quay wall was reduced by nearly 20 m. Bending about the strong axis is also shown by the higher tensile strains in the upper flange (L_{Top} and R_{top})

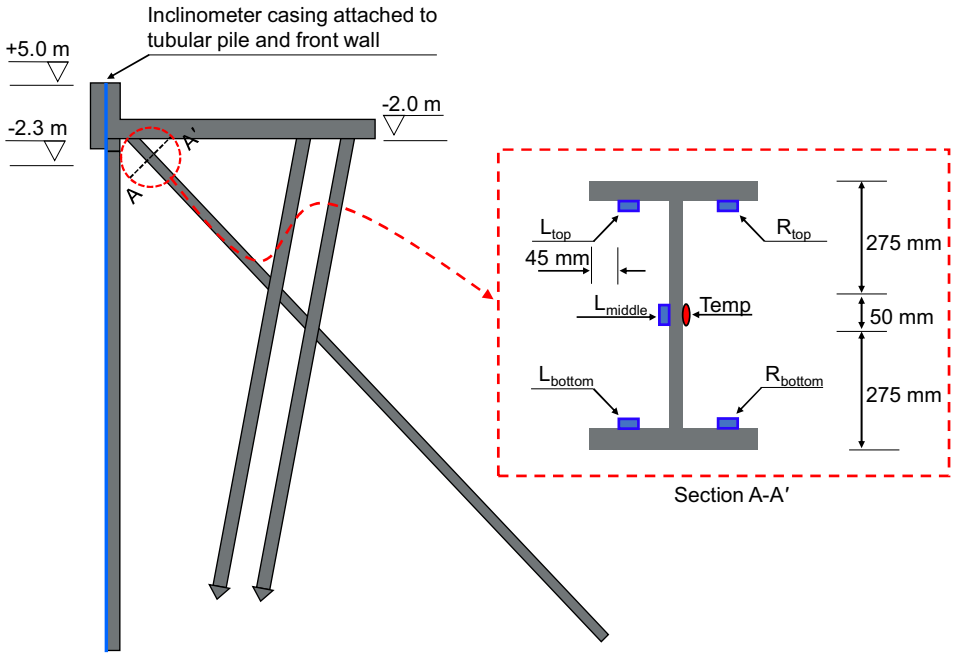

Fig. 7. Cross section of the MV pile with FBG sensors.

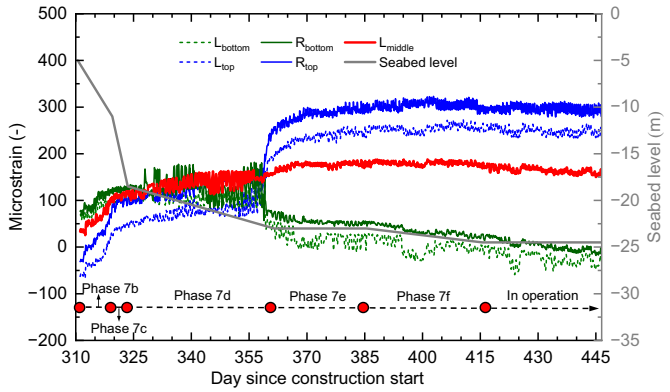

Fig. 8. Measured strains from FBG sensors mounted at the top of the MV pile.

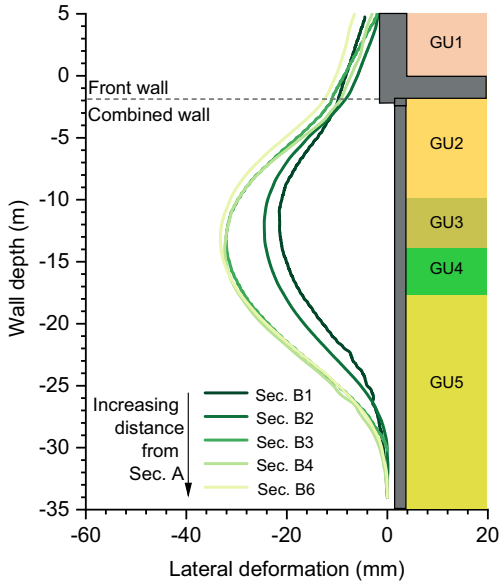

Fig. 9. Postconstruction inclinometer measurements at each quay wall section going from Section A (dredged depth of −19.5 m) to Section B4 (dredged depth of −24.5 m).

compared to the lower flange (L_{bottom} and R_{bottom}). These measurements are symmetrical about the reading made in the web (L_{Middle}).

Regarding the deformation measurements, inclinometer readings were made at several quay wall sections after the construction (Fig. 9). Measurements within the vicinity of Section B4 (i.e., Section B3 and Section B6) show strong agreement with one another for most of retaining height, particularly in terms of the point of maximum deformation. However, the deformations in the front wall (above −2 m) deviate somewhat, with the uppermost deformation measurement ranging from 3 to 8 mm across Sections B3, B4, and B6. The quay wall exhibits a high horizontal stiffness because of the large concrete relieving platform and the interlocking between adjacent segments. This structural behavior is corroborated by the observations in Fig. 9, whereby the point of maximum deformation quickly decreases from 32 to 21 mm as the dredged depth increases from −24.5 m halfway through Section B2 to −19.5 m across Section A. No clear trends in the deformation in the front wall are evident across this transition.

Numerical Modelling

Geometry, Mesh, Boundary Conditions, and Modelling Steps

All numerical simulations were performed with the finite element software PLAXIS 2D 2020 (Bentley Systems). To avoid the influence of boundary effects, the dimensions of the numerical model (Fig. 10) were set as 240 m in width and 55 m in depth. The computational domain was discretized into 15-noded triangular solid elements with a fourth-order shape function.

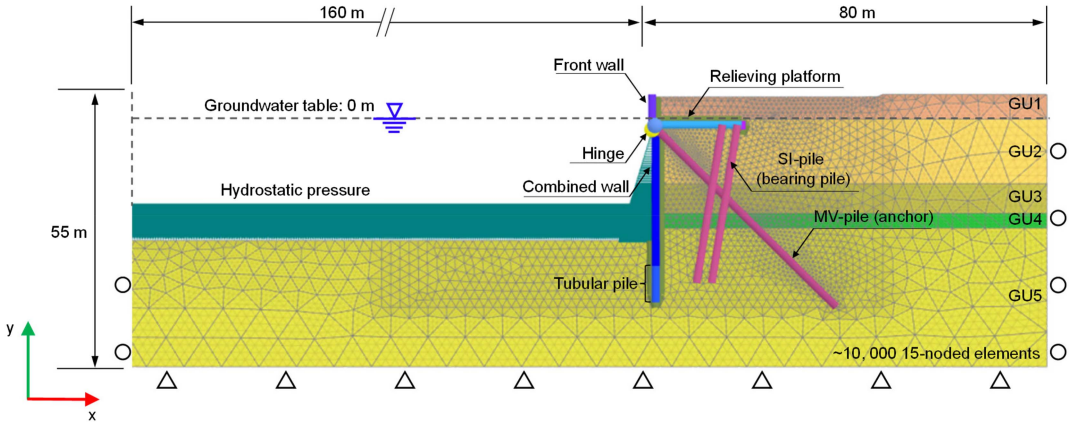

Fig. 10. Geometry, finite element mesh, and boundary conditions.

In terms of boundary conditions, no lateral displacement was allowed on the vertical boundaries ($\Delta x = 0$; $\Delta y \neq 0$), the bottom boundary was horizontally and vertically constrained ($\Delta x = 0$; $\Delta y = 0$) and the top boundary was set as free ($\Delta x \neq 0$; $\Delta y \neq 0$). For the flow conditions, the bottom of the model was closed to prevent flow across it, while the lateral boundaries allowed seepage. A finer mesh was used near the quay wall itself, where high-stress gradients were expected due to the presence of structural elements. The final finite element mesh consisted of 10,629 elements with 86,502 nodes.

The construction sequence in Fig. 6 was replicated in the numerical model. Since the ground had a natural slope before construction, the initial stress field was first generated using gravity loading. Installation of the structural elements (i.e., the combined wall, front wall, MV pile, SI pile, and relieving platform) was considered as wished-in-place. The dredging down to the designated level was performed in stages.

Last, the finite element model used a coupled hydromechanical formulation. In this study, drained conditions were assigned to the sand-dominated layers (GU1, GU2, GU3, and GU5). The clay layer (GU4) was set as undrained, and the undrained strength was determined in terms of effective stress. This means the undrained strength was not a direct input parameter, but instead determined by the constitutive model itself (i.e., effective stress level, stress path, and volumetric behavior). In addition, the ratio of excavation rate to permeability for GU4 is close to 1×10^4, indicating that the undrained analysis without consolidation was sufficient (Uribe-Henao et al. 2023).

Soil Constitutive Model Calibration

To account for the nonlinear degradation of shear stiffness with increasing shear strain during excavation the hardening soil with small strain stiffness (HSS) constitutive model (Schanz et al. 1999; Benz 2007) was used. The HSS model considers shear and compression hardening, implemented with conical and cap yield surfaces.

Advanced laboratory tests on "undisturbed" samples are usually required to determine the input parameters for the HSS model. However, obtaining undisturbed samples in sands and silts is extremely challenging. As an alternative, several different in situ tests were performed around the quay wall to estimate the model parameters for each ground units. The CPTs were used to determine the strength, state and stiffness parameters, while small-strain parameters were determined by the seismic cone penetration test (SCPT) and multichannel analysis of surface waves (MASW).

Based on these tests and a literature review of CPT-based empirical correlations, a unified approach was developed to determine the HSS model parameters (Table 2). The effective soil cohesion (c'), friction angle (ϕ'), unit weight (γ), overconsolidation ratio (OCR), oedometric stiffness (E_{oed}^{ref}), and small strain shear modulus (G_o^{ref}) were grouped as primary model parameters, meaning they could be directly predicted using CPT/CPTU parameters. Other parameters, like the dilation angle (ψ), primary loading stiffness (E_{50}^{ref}, unloading/reloading stiffness (E_{ur}^{ref}), shear strain at 0.7 G_o^{ref} ($\gamma_{0.7}$), stress dependency index (m), and earth pressure coefficient at rest (K_0) were obtained using simplified assumptions because of the difficulties in correlating these parameters to in situ tests.

Fig. 11 plots the shear modulus normalized by the average cone resistance ($G_0/q_{c,avg}$) of various ground units, where G_0 was determined by an MASW survey in the same geological formation but at a nearby site. Average ratios of $\alpha = 4.7$, 6.5, 11.9, and 19.7 were given for GU1 to GU4, respectively. Since the MASW collected a limited number of measurements in GU5, SCPTs from the Dutch North Sea Sector and in the same geological formation (late-Pleistocene Kreftenheye Formation) were used to supplement the results [Fig. 12(a)]. In GU5, the SCPTs yielded a mean velocity profile corresponding to $G_0 = 5.5q_{c,avg}$.

Table 3 presents the HSS model parameters for all soil layers. Using PLAXIS SoilTest, the CPT-based outputs were also compared with laboratory tests on samples from the site. For instance, Fig. 13 presents consolidated drained (CD) triaxial tests under various confining stresses on samples from borehole BH1 at a depth of −28 m (GU5). The numerical results with the HSS model compare well with the experimental results. In addition, for the clay (GU4), the effective friction angle derived from lab triaxial test (ϕ') is around 30°, the mean q_{net} value is 1.8 MPa, and the cone factor N_{kt} is assumed as 15 (Mayne 2008), indicating that the CPT-interpreted undrained strength of 120 kPa agrees well with the computed undrained strength of 119.6 kPa.

Oedometer tests were also modelled in the SoilTest tool and compared to laboratory tests (Fig. 14) on samples from −3.2 m (GU2), −16.2 m (GU3), and −22.0 m (GU4). The corresponding net cone resistances q_{net} are 17.6, 13.8, and 1.8 MPa; and α_m factors are 1.8, 1.8, and 2.1. Of the three stiffness parameters used in the SoilTest tool (E_{oed}^{ref}, E_{50}^{ref}, and E_{ur}^{ref}), E_{oed} was the only correlation, which took CPT measurements as an input, with E_{50} and E_{ur} directly dependent on the value of E_{oed} (Table 2). Using a correlation of $E_{oed} = \alpha_m q_{net}$ gave a good comparison with the laboratory tests across all three ground units.

Table 2. CPT-based correlations to HSS model parameters

Category	Parameter	Correlation	References
Strength parameters	c'	$c' = 0.03\sigma'_{v0}$ (OC soil)	Mayne (2016)
	ϕ'	$\phi' = 17.6 + 11.1\log((q_c/p_a)/(p_a/\sigma_{v0})^{0.5})$ (coarse-grained soil)	Lunne et al. (2002)
		$\phi' = 29.5B_q^{0.121}[0.256 + 0.336B_q + \log Q]$	Mayne (2006)
		$B_q = (u_2 - u_0)/(q_t - \sigma_{v0})$	
		$Q = (q_t - \sigma_{v0})/\sigma'_{v0}$ (fine-grained soil)	
	ψ'	$\psi' = -2 + 12.5D_r/100$; $D_r^2 = (q_c/p_a)/[350(\sigma'_{v0}/p_a)^{0.5}]$ (coarse-grained soil)	Brinkgreve et al. (2010)
		$\psi' = \phi' - 30°$ (fine-grained soil)	Desrues et al. (2000)
State parameters	γ	$\gamma = [0.27\log R_f + 0.36\log(q_t/p_a) + 1.236]\gamma_w$	Robertson and Cabal (2010)
	K_0	$K_0 = K_{0,NC} \cdot OCR^{\sin\phi'}$	Mayne and Kulhawy (1982)
	OCR	$OCR = 0.32(q_t - \sigma_{v0})^{0.72}/\sigma'_{v0}$ (coarse-grained soil)	Agaiby and Mayne (2019)
		$OCR = 0.33(q_t - \sigma_{v0})/\sigma'_{v0}$ (fine-grained soil)	
Stiffness parameters	E_{oed}^{ref}	$E_{oed} = \alpha_M(q_t - \sigma_{v0})$	Robertson (2009)
		$\alpha_M = Q_{tn}(I_c > 2.2$ and $Q_{tn} \le 14)$	
		$\alpha_M = 14(I_c > 2.2$ and $Q_{tn} > 14)$	
		$\alpha_M = 0.03[10^{(0.55Ic+1.68)}](I_c \le 2.2)$	
	E_{50}^{ref}	$E_{50}^{ref} = E_{oed}^{ref}$ (coarse-grained soil)	Schmüdderich et al. (2020)
		$E_{50}^{ref} = 2E_{oed}^{ref}$ (fine-grained soil)	
	E_{ur}^{ref}	$E_{ur}^{ref} = 3E_{oed}^{ref}$ (medium-dense/dense coarse-grained soil)	Schmüdderich et al. (2020)
		$E_{ur}^{ref} = 4E_{oed}^{ref}$ (loose coarse-grained soil)	
		$E_{ur}^{ref} = 5E_{oed}^{ref}$ (fine-grained soil)	
	m	$m = 0.7 - D_r/320$ (coarse-grained soil)	Brinkgreve et al. (2010) and Murphy et al. (2018)
		$m = 1.0$ (fine-grained soil)	
	$\gamma_{0.7}^*$	$\gamma_{0.7} = 0.107G_0 \cdot [2c'(1 + \cos 2\phi') + \sigma'_{v0}(1 + K_0)\sin 2\phi')]$	Benz (2007)
	G_0^{ref*}	$G_0 = \alpha \cdot q_c = \rho v_s^2$ (α is an undetermined coefficient)	—

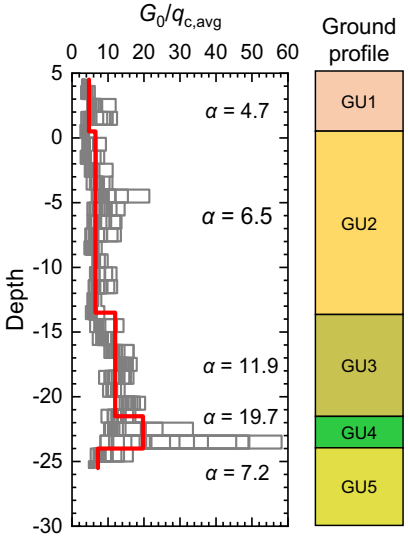

Fig. 11. Correlation between shear modulus and mean cone resistance for various ground units derived from MASW tests.

After obtaining G_0^{ref}, the G_0 profile at various depths (i.e., stress levels) was determined using

$$G_0 = G_0^{ref}\left[\frac{c'\cos\phi' + \sigma'_3\sin\phi'}{c'\cos\phi' + p^{ref}\sin\phi'}\right]^m \quad (1)$$

This same profile can be converted to a V_s profile to compare the numerical predictions with the SCPT results. Good agreement between the measurements and the predictions was shown [Fig. 12(b)], indicating that $G_0 = \alpha q_{c,avg}$ can be used to accurately predict small-strain stiffness. The comparisons made here show that HSS model parameters estimated with CPT results can be used for numerical analyses with reasonable confidence.

Consideration of Structural and Interface Elements

The combined wall, front wall, relieving platform, and hinge support were all modelled using five-noded Mindlin plate elements with a linear-elastic constitutive model. The upper and lower parts of the combined wall were modelled separately since the tubular piles have a larger embedded depth than the sheet piles [Fig. 2(b)], and therefore the drainage conditions and stiffness parameters were different for the impermeable upper part and permeable lower part. Both parts were simulated as a continuous plate element with an equivalent axial and bending stiffness to the combined wall (Table 4), assuming that the lower part benefits from arching across the tubular piles (De Gijt and Broeken 2013). For the SI piles, the bending and axial stiffnesses were derived from the composite concrete–steel stiffness. For the MV piles, it was assumed that all of the stiffness contribution under tensile loading came from steel body.

The MV piles and SI piles were simulated as an embedded pile row (Sluis et al. 2014) so that out-of-plane interaction effects could be accounted for in a 2D space. The input of lateral resistance of piles was set as unlimited, given the small lateral load in relation to the total capacity. The inputs for the axial resistance (i.e., the pile

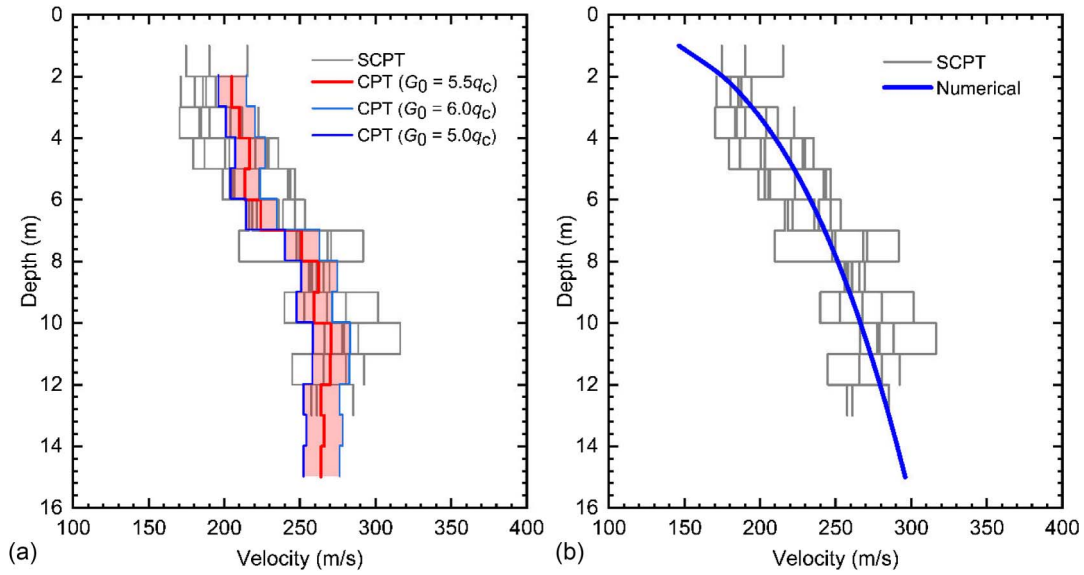

Fig. 12. Comparison of shear wave velocity in GU5: (a) CPT versus SCPT measurements; and (b) SCPT measurements versus numerical simulation.

Table 3. HSS model parameters used in this study

Parameter	Description	Soil layer				
		GU1	GU2	GU3	GU4	GU5
	Strength parameters					
c′ (kPa)	Effective cohesion	0	0	0	0	0
ϕ' (°)	Effective friction angle	40	41	37	30	40
ψ' (°)	Dilation angle	5	6	4	0	6
	Stiffness parameters					
E_{50}^{ref} (MPa)	Primary loading stiffness (reference)	17.3	26.6	11.8	2.5	27.2
E_{oed}^{ref} (MPa)	Oedometric stiffness (reference)	17.3	26.6	11.8	2.2	27.2
E_{ur}^{ref} (MPa)	Un/reloading stiffness (reference)	51.9	79.9	35.5	10.1	81.6
v_{ur} (-)	Un/reloading Poisson's ratio	0.2	0.2	0.2	0.2	0.2
m (-)	Stress dependency index	0.5	0.5	0.6	1.0	0.5
G_0^{ref} (MPa)	Small-strain shear modulus (reference)	80.9	168.8	130.9	33.9	130.9
$\gamma_{0.7}$ (-)	Shear strain at $G_s = 0.722G_0$	2.1E-4	1.8E-4	2.7E-4	7.2E-4	3.7E-4
	Other basic parameters					
p^{ref} (kPa)	Reference stress	100	100	100	100	100
OCR	Overconsolidation ratio	1.0	1.0	1.0	1.5	1.3
γ (kPa)	Unit weight	18.3	20.0	19.6	18.1	20.7
K_0^{nc}	Earth pressure coefficient under NC conditions	0.364	0.347	0.402	0.500	0.354
K_0	Earth pressure coefficient at rest	0.364	0.347	0.402	0.612	0.419
R_{inter}	Strength reduction in interface element	0.90	0.80	0.80	0.80	0.80

Note: GU1 = drained, 5.0 m top level; GU2 = drained, 0.0 m top level; GU3 = drained, −13 m top level; GU4 = undrained, −19.0 m top level; and GU5 = drained, −22.0 m top level.

base resistance F_{max} and shaft resistance T_{max}) were estimated using

$$F_{max} = \alpha_p \cdot q_{c,avg} A_{tip} \quad (2)$$

$$T_{max} = \alpha_s \cdot q_c \cdot A_{circumference} \quad (3)$$

where α_p and α_s = pile class factors that are chosen based on the soil type and installation method; $q_{c,avg}$ = a weighted average of cone resistances around the pile tip determined using the filter method (Boulanger and DeJong 2018); A_{tip} = the contact area between pile base and soil (0.57 m^2 for the SI piles); and $A_{circumference}$ = the surface area of the pile shaft (2.67 and 2.32 m^2 for the SI piles and MV piles respectively).

For the quay wall, the values of α_p and α_s were taken from instrumented load tests on SI piles (Duffy et al. 2024a, b) and MV piles (Westerbeke 2021; Duffy et al. 2024c) with both sets of tests performed in the same geological conditions as the quay wall. Based on these tests, an α_s of 0.012 was used for the SI and MV piles, and an α_p of 0.35 was used for the SI piles.

The interface element with a strength reduction factor R_{inter} (Table 3) accounts for soil–structure interaction. For GU1, the sand–concrete interface of the front wall was considered with $R_{inter} = 0.9$; and for GU2, GU3, and GU5, the steel–sand interface was represented by $R_{inter} = 0.8$ (De Gijt and Broeken 2013; Han et al. 2018; CROW 2023). For GU4 a value of 0.8 was also used, based on recommendations for stiff clay–steel interfaces (NAVFAC 1984). In addition, the option of gap closure was adopted for the interface

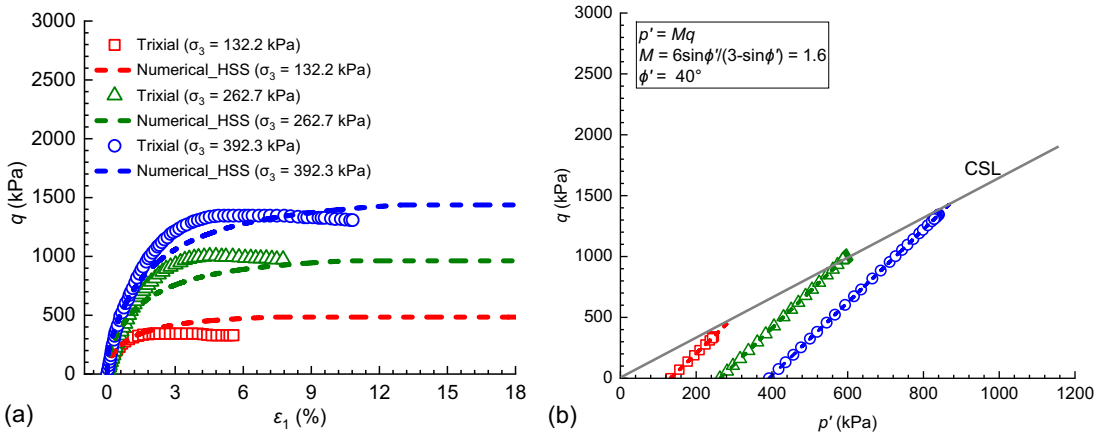

Fig. 13. Comparison of a triaxial test performed in the laboratory and in PLAXIS SoilTest for GU5: (a) $q - \varepsilon_1$ plane; and (b) $q - \varepsilon_1$ plane.

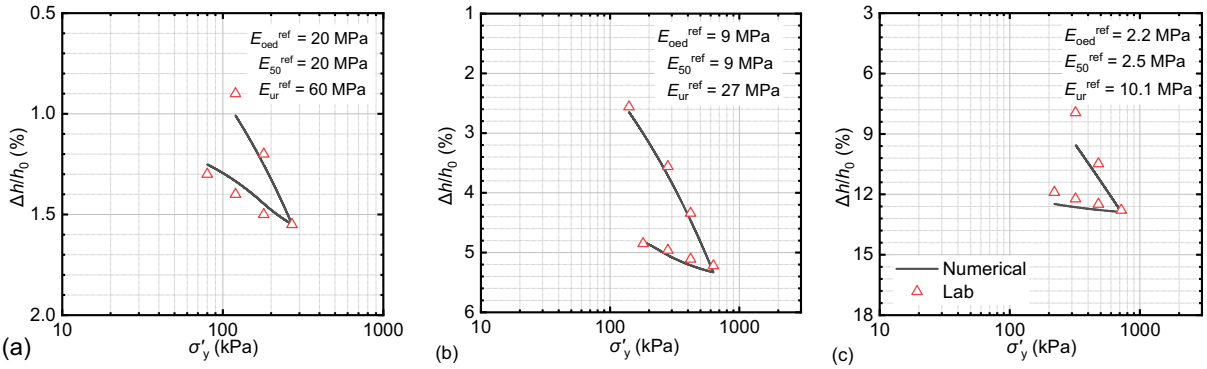

Fig. 14. Comparison of oedometer strain-axial stress results performed in the laboratory and the PLAXIS SoilTest in: (a) GU2; (b) GU3; and (c) GU4.

Table 4. Input parameters of the plate elements used in this study

Plate elements	Axial stiffness, EA (GN/m)	Bending stiffness, EI (GN · m²/m)	Poisson's ratio ν	Unit weight (kN/m³)
Combined wall	6.41	1.62	0.15	78.5
Tubular pile	6.39	1.56	0.15	78.5
Hinge	2.10×10^5	2.10×10^5	0.15	78.5
Relieving platform	35.00	8.90	0.20	24.0
Front wall	44.00	17.70	0.20	24.0

elements. With this, it means that when the load is reversed, the soil–structure contact needs to be restored before a compressive stress can developed.

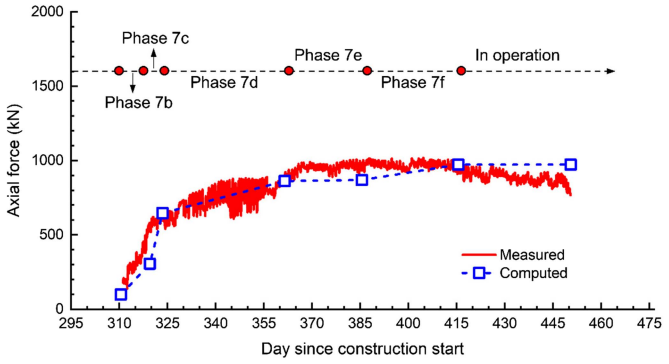

Fig. 15. Comparison of anchor force of MV pile between the numerical and measured results.

Comparison to Monitoring Data

The predictions of the numerical model are compared to the monitoring data by taking the tensile load on the MV pile (Fig. 15). The finite element predictions and the monitoring data match well across all dredging phases, particularly for the first four dredging phases, where 90% of the required dredging was performed (Fig. 6). The total load after all dredging phrases reached just 20% of the design load for the MV piles, although surcharge loading on the quay wall was not yet applied across the measurement period presented.

Fig. 16 compares the computed and measured lateral deformations in the combined wall/front wall at the times closest to Phase 7c and Phase 7f (Fig. 6). The measured deformations were zeroed at the base of the inclinometer casing, making it impossible to measure horizontal displacement of the wall base. As a result, the horizontal displacement measured at the base of the wall was set to the same as that of the numerical model. Fig. 16 shows that the computed deformations are in agreement with the absolute measurement for Phase 7c, where the dredged depth was −18.5 m across the entire quay wall.

After the dredged level at Section B4 was reduced to −24.5 m for Phase 7f, the measurements and predictions are comparable to one another across the combined wall. However, deformations at the top of the front wall are overestimated by 10 mm. This deviation may reflect the horizontal stiffness in the −23 m long concrete

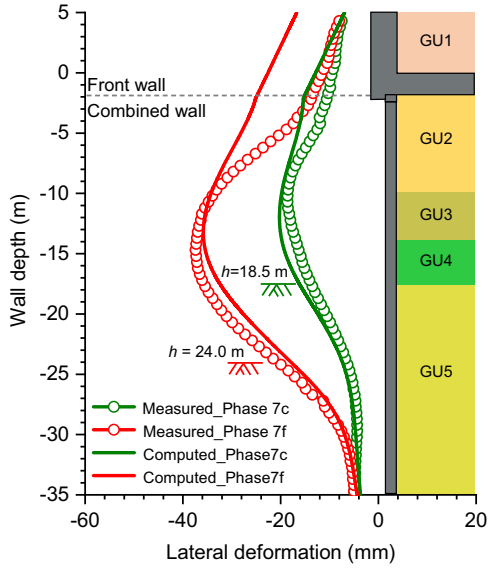

Fig. 16. Lateral deformation of the combined wall/front wall from the numerical and monitoring results.

sections of the front wall itself, particularly since Section B4 was 60 m away Section A, where the dredged depth was 5 m shallower (Fig. 1). A sensitivity analysis was also performed on the rotational stiffness of the hinge joint, as well as setting the joint to fixed, although only minor changes in the deformations at the top of the wall were observed. Nevertheless, the response of this joint should be considered carefully in future work on similar structures, particularly given the uncertainty regarding its true response.

Parametric Study: Influence of Dredging Depth and Surcharge Loading

The seabed depth in front of a quay wall may change over time due to sedimentation (McAnally et al. 2007; Buisman et al. 2024) or scouring (Roubos et al. 2018; Yuksel et al. 2019). Likewise, evaluating the potential for quay wall expansion, either by dredging deeper to host larger ships or by changing the surcharge loads without strengthening the wall, is a critical component for a port authority's asset management plans.

Figs. 17 and 18 show the influence of dredged seabed depth (h) and surcharge loading (q) on the lateral deformation and bending moment of the combined wall/front wall, respectively. The solid line represents the base case, the dotted line represents the quay wall in operation and the dashed line indicates hypothetical scenarios computed by the numerical model. When the dredged depth is increased from 24.5 to 30.5 m [Fig. 17(a)], the maximum wall deformation increases from 35 to 90 mm, with the deformation at the top of the front wall increasing by about 23 mm. A similar trend can also be found in Fig. 18(a) with the maximum negative bending moment (tension toward the waterside) varying from −580 to −930 kN · m/m.

The influence of surcharge loading on the maximum wall deformation and bending moment is less pronounced compared to influence of the dredged depth, likely because of the stress distribution across the relieving platform. Nevertheless, the horizontal deformation of the top of the front wall is comparable in both scenarios, with an increase of 100 kPa in surcharge load leading to an increase of 28 mm in wall deformation [Fig. 17(b)] and an increase of 300 kN · m/m in bending moment [Fig. 18(b)].

Correspondingly, the changes in dredging depth and surface loading also influence the load on the MV pile (Fig. 19). As expected, the axial force of MV pile increases with dredging depth and surcharge loading, for which larger lateral deformations (Fig. 17) and bending moments (Fig. 18) can be observed. The axial force of MV pile follows a linear increase with dredging depth at almost the same rates for different surcharge loads.

Conclusion

Integrating field monitoring and numerical modelling is an efficient way to quantify the reliability of geotechnical structures, providing a basis against which future alterations to the structure can be evaluated. To illustrate this, this paper looks at an instrumented deep-sea quay wall in the port of Rotterdam, using anchor force and wall deformation measurements to show how a reliable 2D finite element model can be established.

In addition, the study used an extensive data set of CPT measurements across the quay wall to derive the input parameters for

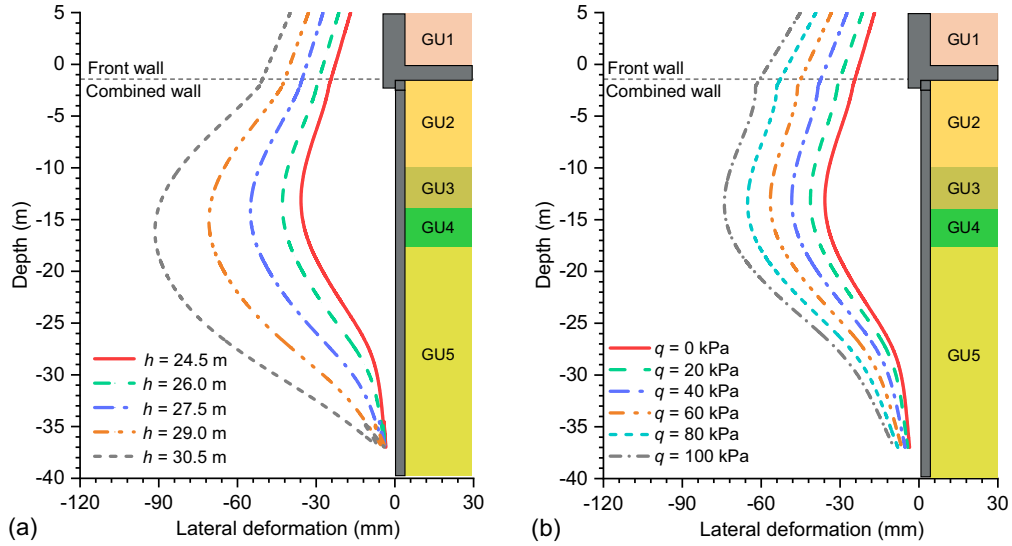

Fig. 17. Influence on lateral wall deformation of: (a) dredging depth; and (b) surcharge loading.

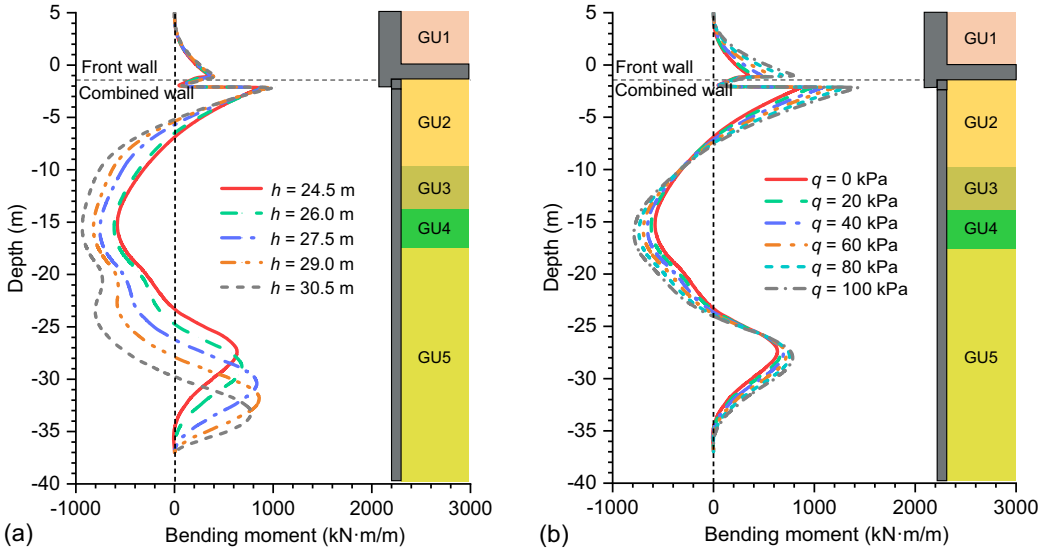

Fig. 18. Influence on bending moment of: (a) dredging depth; and (b) surcharge loading.

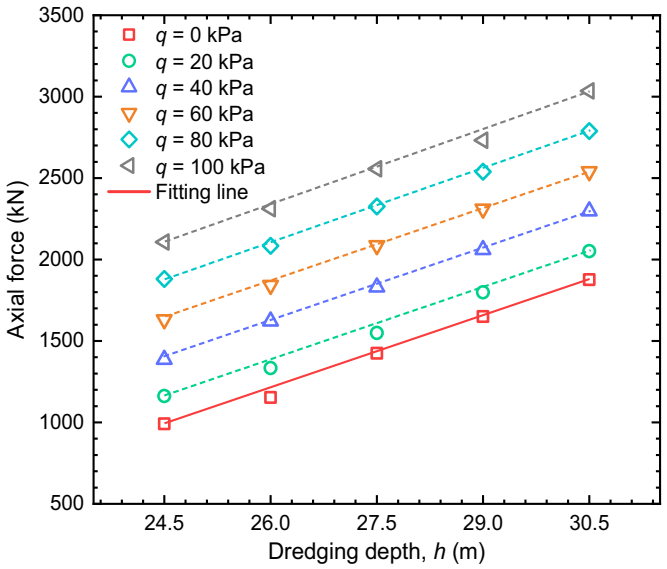

Fig. 19. Influence of the dredging depth and surface loading on the tensile load on the MV pile.

the HSS constitutive model. The approach could capture the quay wall movement during each construction phase, showing that the approach offers a reliable alternative to extensive and complex laboratory test programs across large infrastructural projects. Nevertheless, lateral changes in dredged depth or surcharge loads should be accounted for in the deformation of stiff, continuous foundation elements, such as concrete superstructures.

The numerical model was then used to investigate the influence of hypothetical future changes to the quay wall, namely, the dredged depth in front of the wall and surcharge loading. The findings indicated that wall deformation, bending moment, and anchor force became more pronounced with increased dredging depth and surface loading. Because of the use of a concrete relieving platform behind the quay wall, the dredged depth had more of an influence on the wall deformation compared to changes in surcharge loads.

This study provides a rigorous yet practical CPT-based calibration approach for HSS model parameters, particularly valuable when limited soil data are available. However, the intent is not to replace laboratory testing with CPT, i.e., the final design validation still requires lab test results and potential refinement of the soil constitutive model parameters. This limitation arises because empirical correlations introduce inherent uncertainties, even when high-quality in situ data are used. Future research can build upon this work in several directions: (1) extending the methodology to 3D analyses; (2) developing more generalised in situ test-based approaches for calibrating advanced constitutive models; and (3) investigating long-term performance under changes in applied loads, temperatures, and tides.

Data Availability Statement

All data, models, or codes that support the findings of this study are available from the corresponding author upon reasonable request.

Acknowledgments

Fengwen Lai is supported by the National Natural Science Foundation of China (Grant Nos. 52025084 and 52408356), the China Postdoctoral Science Foundation (Grant Nos. 2025T180886 and 2024M760176), and the Young Elite Scientists Sponsorship Program by CAST (Grant No. 2024QNRC001). The authors are very grateful for the support of the Port of Rotterdam Authority and to MariTeam, Inventec, and Onno Schouten for their assistance in gathering and analyzing the data.

Author Contributions

Fengwen Lai: Formal analysis; Investigation; Software; Validation; Writing – original draft. Kevin Duffy: Data curation; Writing – review and editing. Ken Gavin: Supervision; Writing – review and editing. Dechun Lu: Writing – review and editing. Alfred Roubos: Project administration.

References

Agaiby, S. S., and P. W. Mayne. 2019. "CPT evaluation of yield stress profiles in soils." *J. Geotech. Geoenviron. Eng.* 145 (12): 04019104. https://doi.org/10.1061/(ASCE)GT.1943-5606.0002164.

Alesiani, P., and P. Ruggeri. 2024. "Assessment of load test results on a sheet pile quay wall: The potential of 3D numerical modeling." *J. Geotech. Geoenviron. Eng.* 150 (9): 05024007. https://doi.org/10.1061/JGGEFK.GTENG-12368.

Benz, T. 2007. "Small-strain stiffness of soils and its numerical consequences." Ph.D. thesis, Institute of Geotechnical Engineering, Univ. of Stuttgart.

Boulanger, R. W., and J. T. DeJong. 2018. "Inverse filtering procedure to correct cone penetration data for thin-layer and transition effects." In *Proc., Cone Penetration Testing 2018*, 25–44. Boca Raton, FL: CRC Press.

Brinkgreve, R., E. Engin, and H. K. Engin. 2010. "Validation of empirical formulas to derive model parameters for sands." In *Proc., 7th European Conf. on Numerical Methods in Geotechnical Engineering*, 137–142, Boca Raton, FL: CRC Press.

Brinkgreve, R. B., and S. Brasile. 2022. "Automatic finite element modelling and parameter determination for geotechnical design." In Vol. 53 of *Proc., Workshop Numerische Methoden in der Geotechnik*, 83–97. Hamburg, Germany: Institute of Geotechnical Engineering and Construction Management, Hamburg Univ. of Technology.

Buisman, M., D. Draganov, and A. Kirichek. 2024. "Near real-time nautical depth mapping via horizontal optical fibers and distributed acoustic sensing." *J. Appl. Geophys.* 225 (Jun): 105377. https://doi.org/10.1016/j.jappgeo.2024.105377.

CROW (Centre for Regulation and Research). 2023. *CUR Handboek 166: Damwandconstructies (deel 1 and 2) [CUR handbook: Retaining walls (Part 1 and 2)]*. [In Dutch.] Ede, Netherlands: CROW.

De Gijt, J. G. 2010. "A history of quay walls: Techniques, types, costs and future." Ph.D. thesis, Faculty of Civil Engineering and Geosciences, Delft Univ. of Technology.

De Gijt, J. G., and M. Broeken. 2013. *Quay walls*. 2nd ed. Boca Raton, FL: CRC Press.

Desrues, J., B. Zweschper, and P. Vermeer. 2000. *Database for tests on Hostun RF sand*. Stuttgart, Germany: Institute of Geotechnik, Univ. of Stuttgart.

Duffy, K., K. Gavin, M. Korff, and D. de Lange. 2024a. "Base resistance of screw displacement piles in sand." *J. Geotech. Geoenviron. Eng.* 150 (8): 04024070. https://doi.org/10.1061/JGGEFK.GTENG-12340.

Duffy, K., K. Gavin, M. Korff, D. de Lange, and A. Roubos. 2024b. "Influence of installation method on the axial capacity of piles in very dense sand." *J. Geotech. Geoenviron. Eng.* 150 (6): 04024043. https://doi.org/10.1061/JGGEFK.GTENG-12026.

Duffy, K., K. G. Gavin, and F. Lai. 2024c. "Maximising a foundation's lifetime through monitoring: A case study from the Port of Rotterdam." In *Proc., 2nd Annual Conf. on Foundation Decarbonization and Re-Use*, 1–9. Amsterdam, Netherlands: Royal Tropical Institute.

Feremans, G., and R. Vanhooydonck. 2019. "Full scale load test on historic quay wall in Antwerp." In *Proc., 17th European Conf. on Soil Mechanics and Geotechnical Engineering*, London: International Society for Soil Mechanics and Geotechnical Engineering.

Han, F., E. Ganju, R. Salgado, and M. Prezzi. 2018. "Effects of interface roughness, particle geometry, and gradation on the sand–steel interface friction angle." *J. Geotech. Geoenviron. Eng.* 144 (12): 04018096. https://doi.org/10.1061/(ASCE)GT.1943-5606.0001990.

Hemel, M. 2023. "Amsterdam quays under pressure: Modelling and testing of historic canal walls." Ph.D. thesis, Faculty of Civil Engineering and Geosciences, Delft Univ. of Technology.

Kim, J.-M., C.-M. Kim, S.-Y. Choi, and B. Y. Lee. 2017. "Enhanced strain measurement range of an FBG sensor embedded in seven-wire steel strands." *Sensors* 17 (7): 1654. https://doi.org/10.3390/s17071654.

Lai, F., S. Liu, J. Shiau, M. Liu, G. Cai, and M. Huang. 2025a. "Data-driven modeling for evaluating deformation responses of a deep excavation near existing tunnels." *Underground Space* 24 (10): 162–179. https://doi.org/10.1016/j.undsp.2025.04.003.

Lai, F., F. Tschuchnigg, H. F. Schweiger, S. Liu, J. Shiau, and G. Cai. 2025b. "A numerical study of deep excavations adjacent to existing tunnels: Integrating CPTU and SDMT to calibrate soil constitutive model." *Can. Geotech. J.* 62 (Feb): 1–23. https://doi.org/10.1139/cgj-2024-0203.

Lai, F., N. Zhang, S. Liu, Y. Sun, and Y. Li. 2021. "Ground movements induced by installation of twin large diameter deeply-buried caissons: 3D numerical modeling." *Acta Geotech.* 16 (Mar): 2933–2961. https://doi.org/10.1007/s11440-021-01165-1.

Lunne, T., J. J. Powell, and P. K. Robertson. 2002. *Cone penetration testing in geotechnical practice*. Boca Raton, FL: CRC Press.

Mayne, P. 2016. "Evaluating effective stress parameters and undrained shear strengths of soft-firm clays from CPT and DMT." *Aust. Geomech. J.* 51 (4): 27–55.

Mayne, P. W. 2007. "In-situ test calibrations for evaluating soil parameters." In Vol. 3 of *Characterization & engineering properties of natural soils*, 1602–1652. Singapore: Taylor & Francis Group.

Mayne, P. W. 2008. "Piezocone profiling of clays for maritime site investigations." In *Proc., 11th Baltic Sea Geotechnical Conf.*, 15–18. Gdańsk, Poland: Gdańsk Univ. of Technology.

Mayne, P. W., and F. H. Kulhawy. 1982. "Ko-OCR relationships in soil." *J. Geotech. Eng. Div.* 108 (6): 851–872. https://doi.org/10.1061/AJGEB6.0001306.

McAnally, W. H., C. Friedrichs, D. Hamilton, E. Hayter, P. Shrestha, H. Rodriguez, A. Sheremet, and A. Teeter. 2007. "Management of fluid mud in estuaries, bays, and lakes. I: Present state of understanding on character and behavior." *J. Hydraul. Eng.* 133 (1): 9–22. https://doi.org/10.1061/(ASCE)0733-9429(2007)133:1(9).

Murphy, G., D. Igoe, P. Doherty, and K. Gavin. 2018. "3D FEM approach for laterally loaded monopile design." *Comput. Geotech.* 100 (Aug): 76–83. https://doi.org/10.1016/j.compgeo.2018.03.013.

NAVFAC (Naval Facilities Engineering Systems Command). 1984. *Foundations and Earth structures*. Rep. No. DM 7.02. Washington, DC: US Dept. of the Navy.

Qiu, G., and J. Grabe. 2012. "Active earth pressure shielding in quay wall constructions: Numerical modeling." *Acta Geotech.* 7 (4): 343–355. https://doi.org/10.1007/s11440-012-0186-3.

Robertson, P. K. 2009. "Interpretation of cone penetration tests—A unified approach." *Can. Geotech. J.* 46 (11): 1337–1355. https://doi.org/10.1139/T09-065.

Robertson, P. K., and K. Cabal. 2010. "Estimating soil unit weight from CPT." In *Proc., 2nd Int. Symp. on Cone Penetration Testing*, 2–40. Martinez, CA: Gregg Drilling & Testing.

Roubos, A., T. Blokland, and T. Van Der Plas. 2018. "Field tests propeller scour along quay wall." In *Proc., PIANC World Congress*. Brussels, Belgium: World Association for Waterborne Transport Infrastructure.

Roubos, A., T. Schweckendiek, R. Brinkgreve, R. Steenbergen, and S. N. Jonkman. 2021. "Finite element-based reliability assessment of quay walls." *Georisk* 15 (3): 165–181. https://doi.org/10.1080/17499518.2020.1756344.

Schanz, T., P. Vermeer, and P. G. Bonnier. 1999. "The hardening soil model: Formulation and verification." In *Beyond 2000 in computational geotechnics*, 281–296. Rotterdam, Netherlands: A. A. Balkema.

Schmüdderich, C., M. M. Shahrabi, M. Taiebat, and A. A. Lavasan. 2020. "Strategies for numerical simulation of cast-in-place piles under axial loading." *Comput. Geotech.* 125 (Sep): 103656. https://doi.org/10.1016/j.compgeo.2020.103656.

Sluis, J., F. Besseling, and P. Stuurwold. 2014. "Modelling of a pile row in a 2D plane strain FE-analysis." In *Numerical methods in geotechnical engineering*, 277–282. Boca Raton, FL: CRC Press.

Stark, T. D., and H. Choi. 2008. "Slope inclinometers for landslides." *Landslides* 5 (3): 339–350. https://doi.org/10.1007/s10346-008-0126-3.

UNCTAD (United Nations Trade and Development). 2023. *Review of maritime transport 2023*. New York: UNCTAD.

Uribe-Henao, A. F., L. G. Arboleda-Monsalve, C. Ballesteros, and D. G. Zapata-Medina. 2023. "Method for estimating fully coupled response of deep excavations in soft clays." *J. Geotech. Geoenviron. Eng.* 149 (5): 04023026. https://doi.org/10.1061/JGGEFK.GTENG-9278.

Voogt, H. 2023. "Port facilities asset management: Coping with aging infrastructure and constrained budgets on the long term." In *Life-cycle of structures and infrastructure systems*, 3642–3648. Boca Raton, FL: CRC Press.

Westerbeke, F. 2021. "Geotechnical bearing capacity of MV piles: Improving the design based on full scale load tests in the Port of Rotterdam." Ph.D. thesis, Faculty of Civil Engineering and Geosciences, Delft Univ. of Technology.

Yuksel, Y., R. I. Tan, and Y. Celikoglu. 2019. "Determining propeller scour near a quay wall." *Ocean Eng.* 188 (Sep): 106331. https://doi.org/10.1016/j.oceaneng.2019.106331.